Supporting information

Interface-Engineered Bi_2O_3/N-Doped Carbon Heterostructure Enabling Synergistic Effects for Advanced Energy Storage

Yuan Wang,[a,#] Zhongtao Shang,[a,#] Tao Zhang,[b] Chen Wu,[c] Yiyang Dai,[a] Shaojun Yuan[a,*]

[a] Low-carbon Technology & Chemical Reaction Engineering Lab, College of Chemical Engineering, Sichuan University, Chengdu 610065, P. R. China
[b] Department of Materials Science and Engineering, City University of Hong Kong, Kowloon Tong, Hong Kong, SAR 999077, P. R. China
[c] Natural Gas Research Institute, PetroChina Southwest Oil & Gasfield Company, Chengdu, Sichuan, 610213, P. R. China.
# These two authors contribute equally.
*Corresponding author: ysj@scu.edu.cn (S.J. Yuan), Tel/fax: +86-28-85405201

S1. Supplementary experimental section

S1.1 Material Characterization.

Morphological and microstructural evaluations were carried out using scanning electron microscopy (SEM, REGULUS 8230) and transmission electron microscopy (TEM) on a Zeiss Libra 200FE microscope, and X-ray photoelectron spectroscopy (XPS, Thermo Scientific K-Alpha, Al Kα). Crystalline structures were analyzed via X-ray diffraction (XRD, Philips Pw1730), and vibrational properties were assessed using Raman spectroscopy (DXR Raman microscope, Thermo Fisher Scientific, λ = 455 nm).

S1.2 Electrochemical measurement.

The electrochemical properties of the prepared electrodes were comprehensively investigated by cyclic voltammetry (CV), galvanostatic charge-discharge (GCD), and electrochemical impedance spectroscopy (EIS), using a CHI660E electrochemical workstation (Chenhua Instruments, Shanghai, China). A Hg/HgO electrode and a platinum sheet were employed as the reference and counter electrodes, respectively. All measurements were conducted in 2 M KOH or 2 M NaOH aqueous electrolyte. The specific capacitance (C_S, mF cm^{-2}) of the electrodes based on CV curve and GCD data was determined through the following Eq. (1) and Eq. (2).

$$C = \int IdV/(2 \times \Delta V \times v \times S) \tag{1}$$

$$C = I \times \Delta t/(S \times \Delta V) \tag{2}$$

Here the $\int IdV$ represents the integrated area of the CV curve, v denotes the scan rate, S indicates the effective surface area of the working electrode, Δt is the discharge time and ΔV stands for the applied potential window. For asymmetric supercapacitor (ASC) system, the specific capacitance (C_S, mF cm^{-2}) was calculated via the following Eq.

(3):

$$C_s = I\,\Delta t/(S \times \Delta V) \quad (3)$$

The areal energy (E_S, mWh cm^{-2}) and power (P_S, mW cm^{-2}) densities of ACSs device were obtained using the following Eq. (4) and Eq. (5):

$$E = 1/2(C/3600)(\Delta V)^2 \quad (4)$$

$$P = E \times 3600/\Delta t \quad (5)$$

S1.3 Calculations of capacitive contribution.

The capacitive and diffusion contributions can be quantitatively determined via separating the current *i* at a fixed potential *V*, the corresponding equations are expressed as the following equations $i(V) = k_1v^{1/2} + k_2v$. *The* $k_1v^{1/2}$ ， the $k_1v^{1/2}$ and k_2v represent the contributions from the diffusion-controlled and capacitive-controlled process, respectively, where k_1 and k_2 can be easily calculated by the $i(V)/v^{1/2} = k_1 + k_2 v^{1/2}$.

S1.2 First-principles calculations.

The calculations are performed on the basis of density functional theory (DFT) with the Vienna Ab initio simulation package VASP.5.4.4 [1]. For the exchange-correlation functional, the generalized gradient approximation (GGA) with Perdew-Burke-Ernzerhof (PBE) form are used. A number of fifteen valence electrons for each Bi atom ($5d^{10}6s^26p^3$), six valence electrons for each O atom ($2s^2p^4$), four valence electrons for each C atom ($2s^2p^2$) and five valence electrons for each N atom ($2s^2p^3$) are taken into account. For adsorbed atoms a number of seven valence electrons for Na atom ($2p^63s^1$) and seven valence electrons for K atom ($3p^64s^1$) are taken into account. The remaining electrons together with the nucleus are described by projector-augmented wave (PAW) pseudopotentials[2]. The one-electron Kohn-Sham

wavefunctions and the charge density are expanded in a plane-wave basis set with cutoff energy 500 eV[3]. The convergence criterion is 10^{-5} eV and 0.01 eV/Å for energy and force, respectively. The Brillouin zone for adsorption systems was divided into a 2 × 2 × 1 mesh of k points from Gamma centered Monkhorst–Pack. Under these parameters setting, the structure parameters (a = b = 8.07 Å, c = 5.73 Å, α = β =γ = 90°) of optimized Bi_2O_3 correspond well with previous study. We select a 4 × 7 graphite (001) supercell and a 2 × 3 Bi_2O_3 (100) supercell to construct a heterojunction interface model of Bi_2O_3/Graphene and Bi_2O_3/N-Graphene heterojunction to simulate the structure of the Bi_2O_3/carbon interface. This heterojunction model has a lattice mismatch rate of less than 5% in both the a and b directions, indicating that the heterojunction meets the requirements for structural stability. A vacuum of 15 Å was included to isolate slabs for reducing the interactions between each slab. The adsorption energies Eads are adopted to describe the Na and K adsorption ability of different interfaces using equation:

$$E_{ads} = E_{total} - E_{interface} - E_{ion}$$

Where the E_{total} is the DFT calculated total energy of the fully optimized composite system with adsorbed atoms (K or Na) on the graphene, pure-Bi_2O_3, and Bi_2O_3/Graphene and Bi_2O_3/N-Graphene, $E_{interface}$ is the total energy of the fully optimized graphene, pure-Bi_2O_3, and Bi_2O_3/graphene structure, E_{ion} is the total energy of a single adsorbed atoms (K or Na) in their corresponding bulk.

S2. Supplementary Results and Discussion

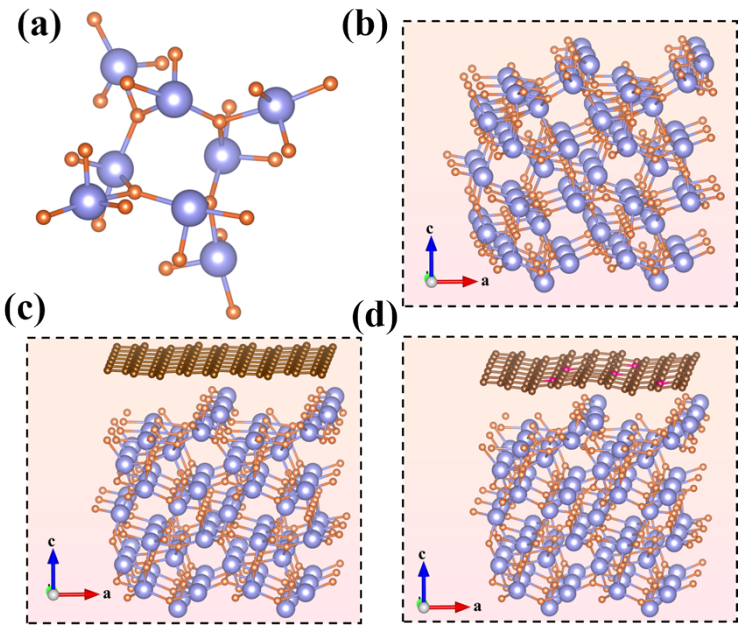

Figure S1. (a) The crystal structure of pristine tetragonal Bi_2O_3. Diagram of optimized structure (b) Bi_2O_3-pure and heterostructures of (c) Bi_2O_3/Graphene and (d) Bi_2O_3/N-Graphene.

The Bi_2O_3-pure model consists of 95 bismuth atoms and 144 oxygen atoms, with the bottom four layers of atoms fixed to mimic the internal state of the Bi_2O_3 electrode. The Bi_2O_3/Graphene and Bi_2O_3/N-Graphene heterojunction model is formed by the integration of Bi_2O_3 (104) and graphene. The single layer of graphene (112 carbon atoms), is stacked onto the surface of Bi_2O_3 (100), with the bottom four layers of the Bi_2O_3 (100) also fixed. The initial interlayer spacing between graphene and Bi_2O_3 (100) is set at adout 4.0 Å. Similarly, a vacuum region of about 15 Å is established in the Z-axis direction to simulate the surface state.

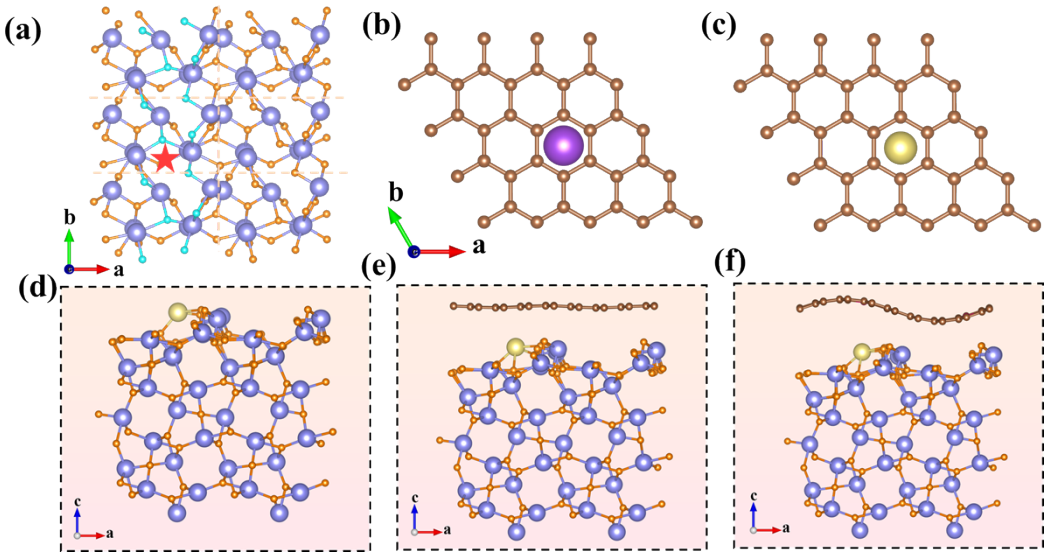

Figure S2. (a) Schematic diagram of adsorption sites. (b) Diagram of the optimized (b) K^+ and (c) Na^+ adsorption in the (001) plane of Graphene. The optimized adsorption configuration of (d) Bi_2O_3-Na^+, Bi_2O_3/Graphene-Na^+ and Bi_2O_3/N-graphene-Na^+.

Taking into account the positions of oxygen atoms on the Bi_2O_3 (100) crystal facet, the periodicity of the facet, and the symmetry, one stable adsorption site was considered. The single-layer graphene model comprises 32 carbon atoms.

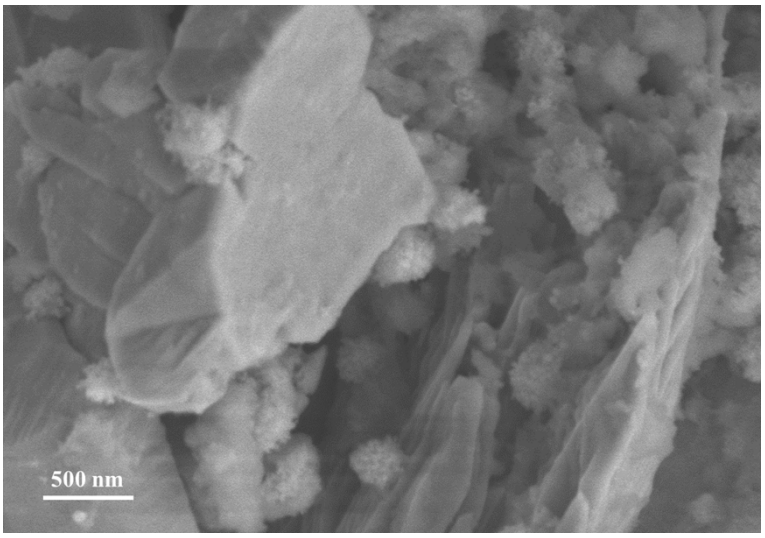

Figure S3 SEM of nano-ZnO particles.

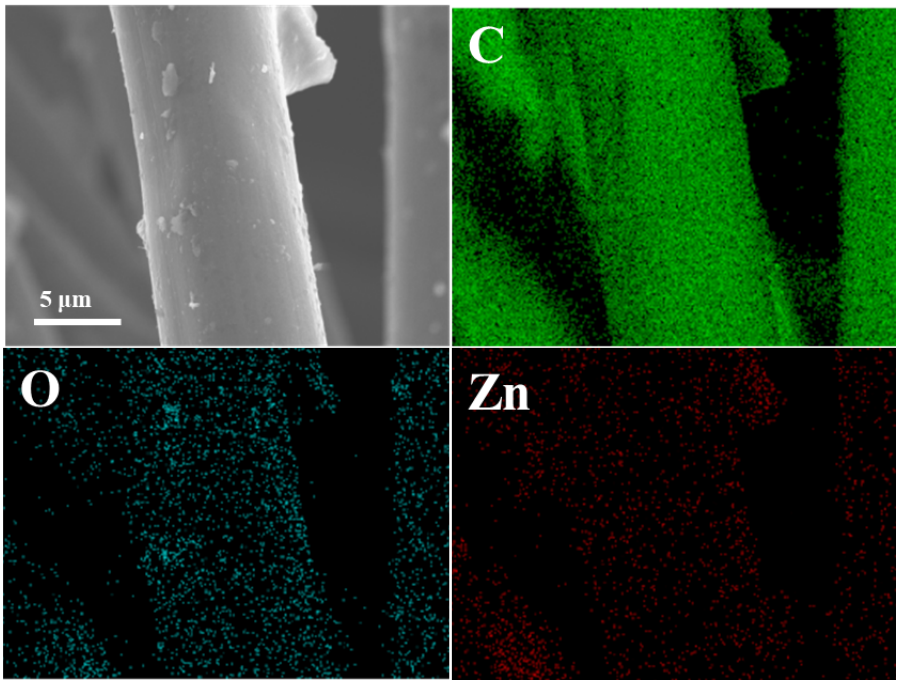

Figure S4 EDS mapping images of the precursor.

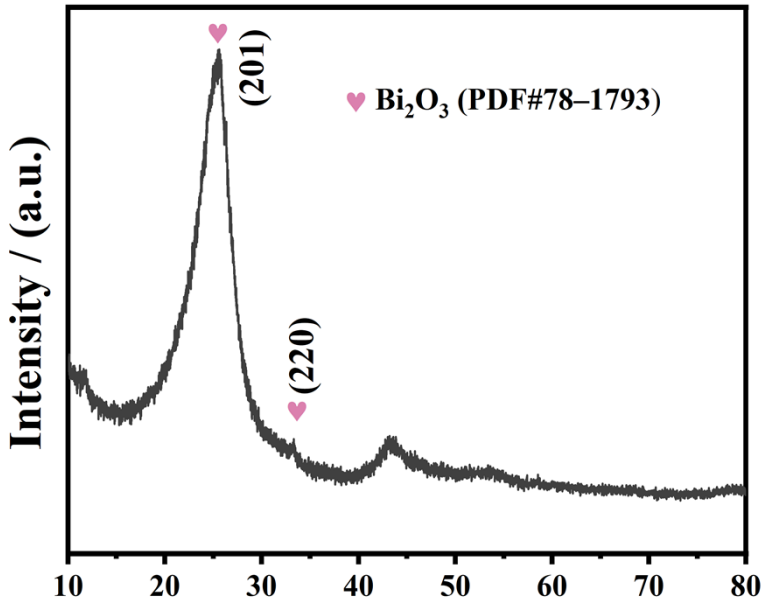

Figure S5 XRD of Bi_2O_3@CC

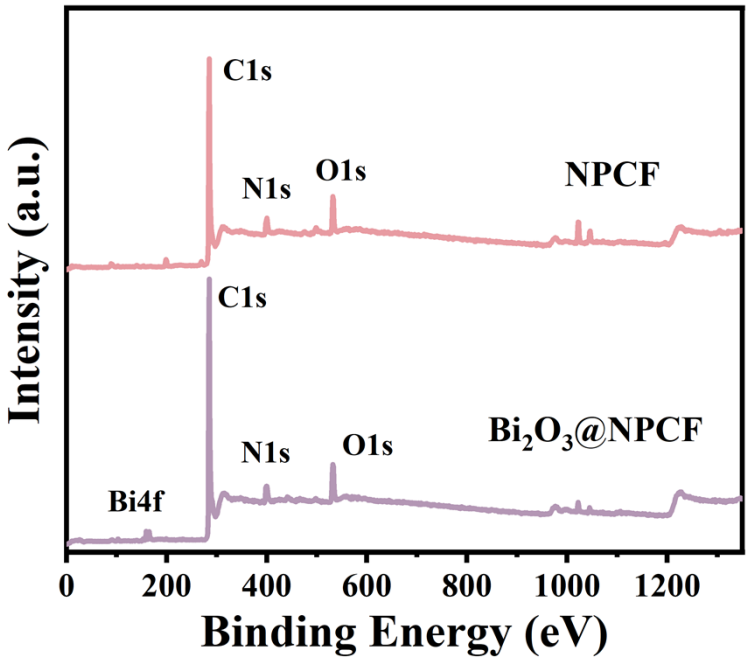

Figure S6. Wide XPS spectrum of NPCF and Bi_2O_3@NPCF.

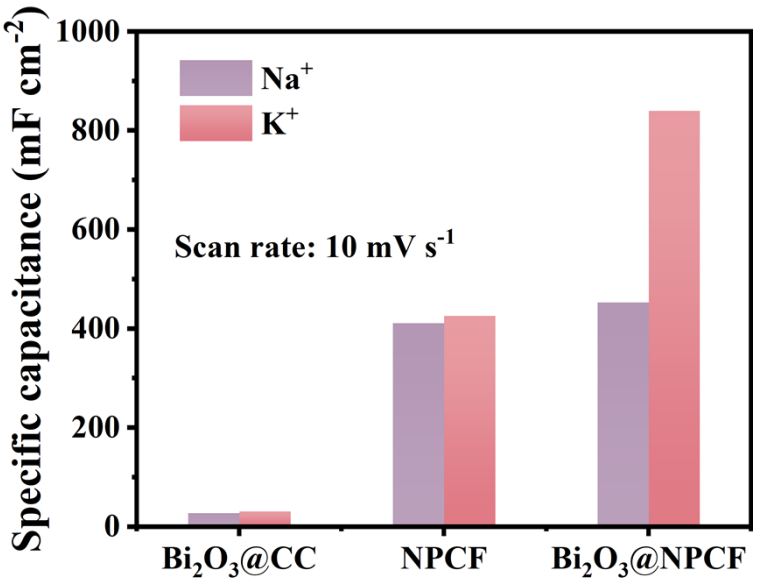

Figure S7. Comparation of the specific capacitance for Bi_2O_3@CC, NPCF and Bi_2O_3@NPCF at the scan rate of 10mV s^{-1}.

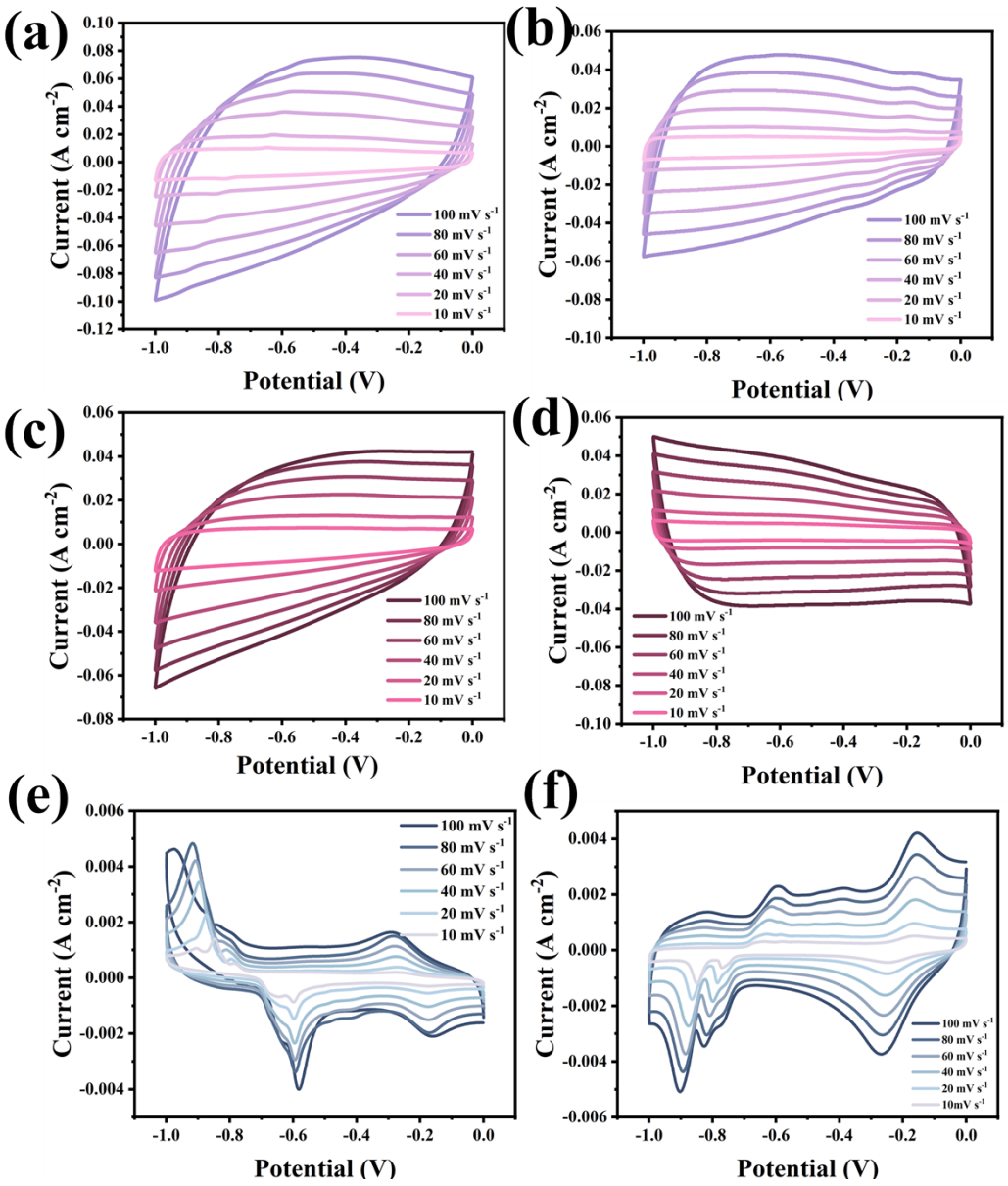

Figure S8. CV curves in 2 M KOH and 2 M NaOH at different scan rates: (a) (b) Bi_2O_3@NPCF, (c) (d)NPCF, (e)(f) Bi_2O_3@CC.

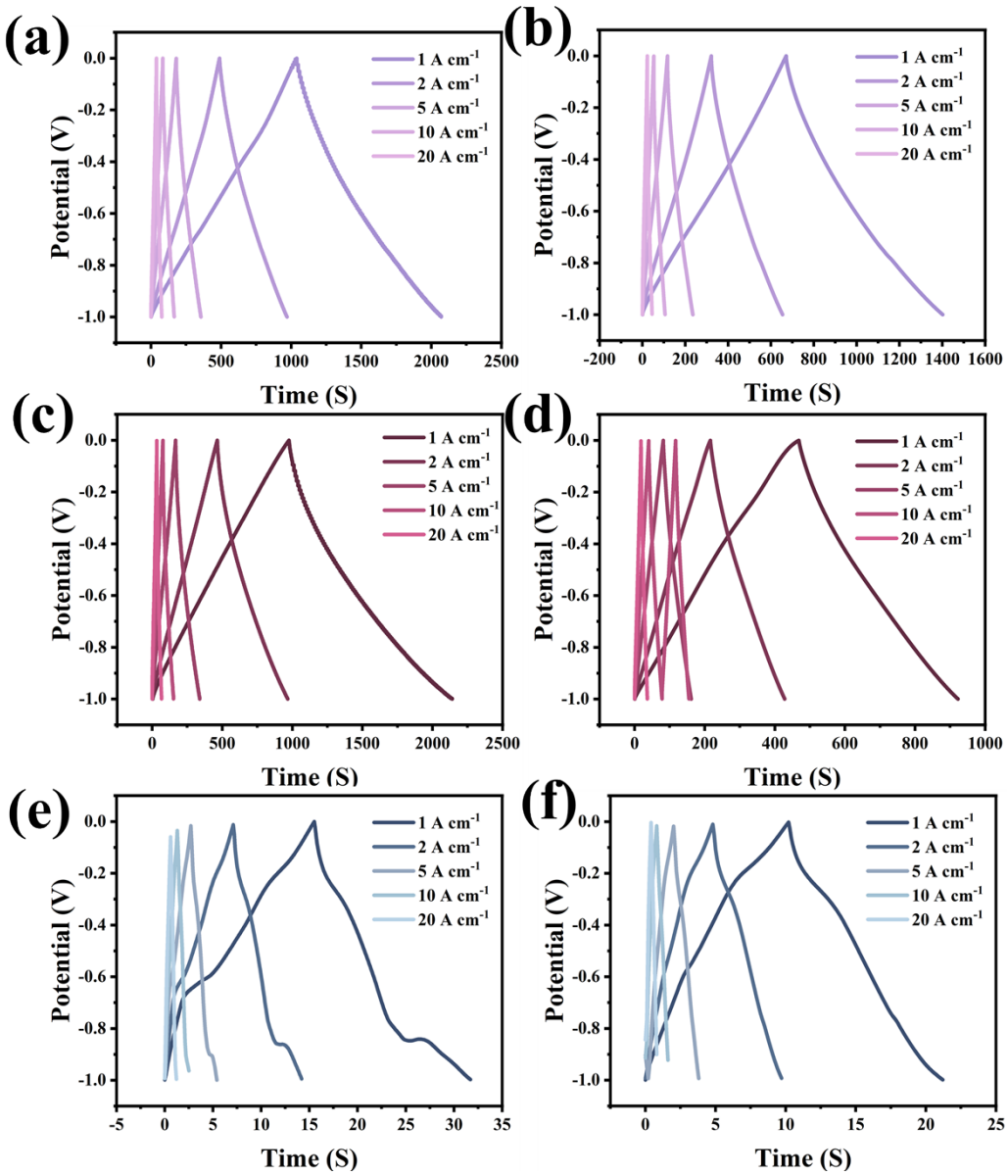

Figure S9 GCD curves in 2 M KOH and 2 M NaOH at different current densities: (a) (b) Bi_2O_3@NPCF, (c) (d)NPCF, (e)(f) Bi_2O_3@CC.

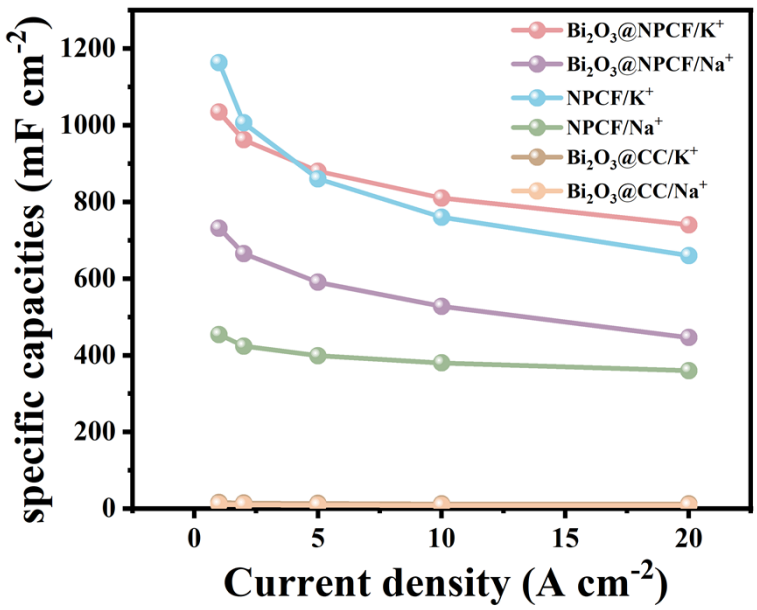

Figure S10 Rate performance of all electrodes based on GCD data in 2 M KOH and 2 M NaOH

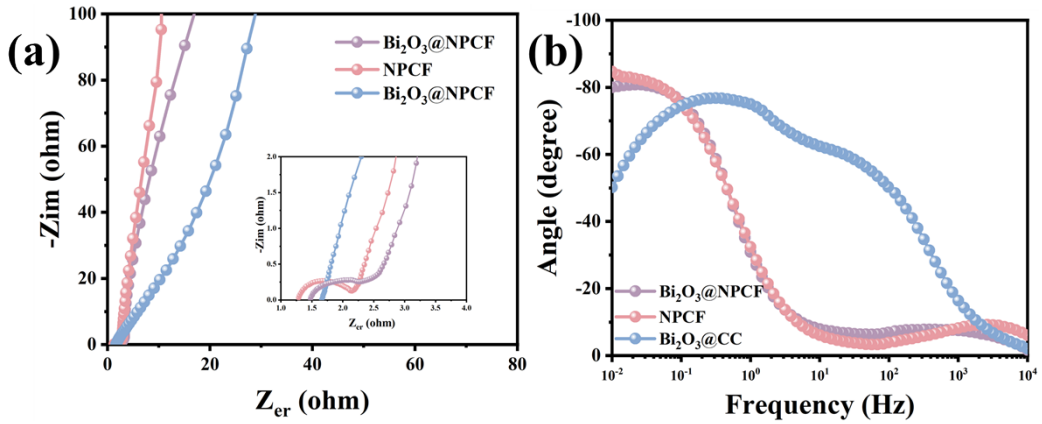

Figure S11. (a) Nyquist plots and (b) Bode phase plots of all samples in 2 M NaOH.

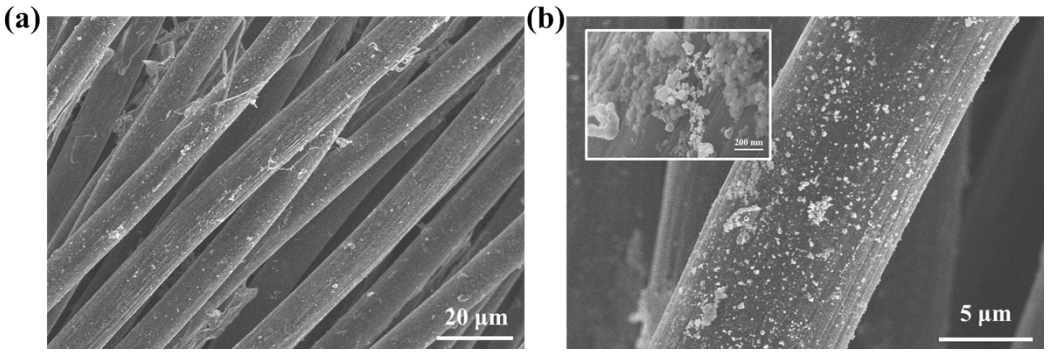

Figure S12. The SEM images of Bi_2O_3@NPCF after long-term cycling: (a) low magnification; (b) high magnification.

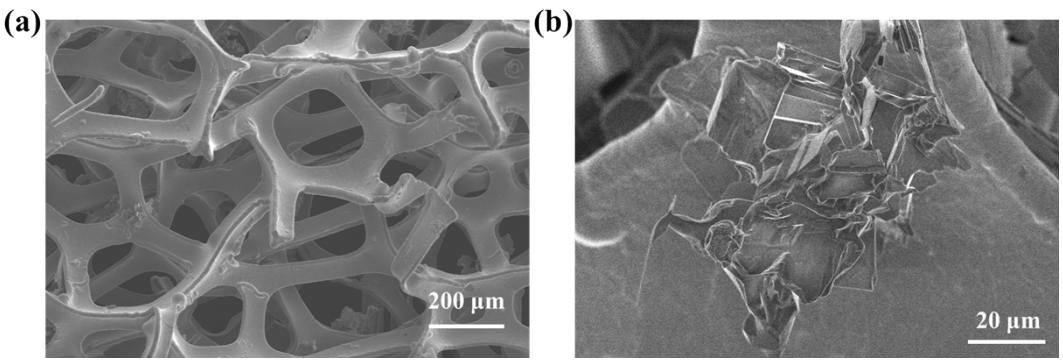

Figure S13. The SEM images of $Co(OH)_2$/Ag electrode : (a) low magnification; (b) high magnification.

The low-magnification SEM image of the $Co(OH)_2$/Ag electrode shows that $Co(OH)_2$/Ag particles are sparsely distributed on the nickel foam substrate, while the corresponding high-magnification image reveals the morphology of the $Co(OH)_2$/Ag structures.

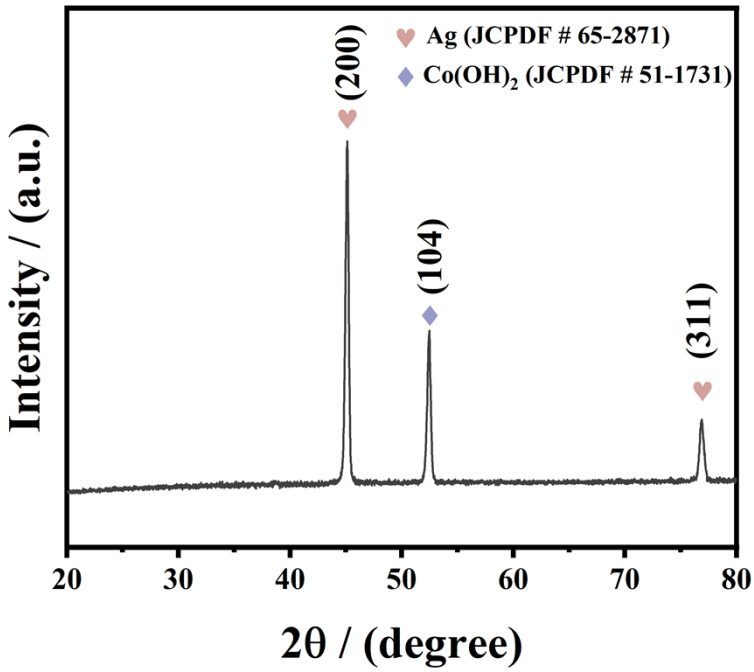

Figure S14. The XRD spectra of $Co(OH)_2$/Ag.

The XD patterns of $Co(OH)_2$/Ag shows the characteristic peaks at 44.3° and 77.4° corresponding to the (200) and (311) of Ag, and the characteristic peaks at 51.6° corresponding to the (104) of $Co(OH)_2$.

Table S1. Electrochemical performance of Bi-based/carbon nanocomposite electrodes for supercapacitors

Electrodes	Electrodes	Potential (V)	Specific capacity	References
Bi_2O_3@NPCF	2 M KOH 2 M NaOH	-1–0	1034.2 mF cm^{-2} (574.5 F g^{-1}) 731.1 mF cm^{-2} (406.1 F g^{-1}) at 1 mA cm^{-2}	**This work**
$Bi_{13}S_{18}I_2$	3 M KOH	-0.4–0.4	247 mF cm^{-2} at 5 mA cm^{-2}	3
Bi_2O_3/CNF	1 M Na_2SO_4	-1–0	0.348 mAh cm^{-2} at 3 mA cm^{-2}	4
AC-Bi_2O_3	6 M KOH	-1–0	332.6 F g^{-1} at 1 A g^{-1}	5
CQD-Bi_2O_3	3 M KOH	-0.75–0	343 F g^{-1} at 0.5 A g^{-1}	6
Bi_2O_3 Nanostructured	6 M KOH	-1–0	447 F·g^{-1} at 2 A·g^{-1}	7
SWCNT/BiVO4	2 M NaOH	-1–0	395 F g−1 at 1 A·g^{-1}	8
Bi_2O_3 nanobelts	1 M Na_2SO_4	-1– -0.2	250 F g−1 at 1 A·g^{-1}	9

Table S2. Electrochemical performance of Bi-based/carbon nanocomposite electrodes for supercapacitors

Electrodes	Electrodes	Potential (V)	Specific capacity	References
Bi_2O_3@NPCF	2 M KOH 2 M NaOH	-1–0	1034.2 mF cm^{-2} (574.5 F g^{-1}) 731.1 mF cm^{-2} (406.1 F g^{-1}) at 1 mA cm^{-2}	This work
Fe_2O_3@PEDOT	1 M Na_2SO_3	-1–0	338 mF cm−2 at 1 mA cm-2	10
V_2O_5/n-MPC	0.5 M K_2SO_4	0–1	487 Fg^{-1} at 0.5 Ag^{-1}	11
Fe_2O_3/HPC	1 M Na2SO4	-1–0	465 F g−1 at 0.5 A g−1	12
MnO_2/CNT	3 M NaCl	0–1	370 F g^{-1} at 0.5 A g^{-1}	13
Ni/NiO/C	3 M KOH	0–0.4	550 F g-1 at 1 A g-1	14
Fe_3O_4@PPy	1M H_2SO_4	0–0.8	290.2 F g-1 1 A g-1	15
Co3O4 @ CSCNs	3 M NaCl	-0.8–0	508 F g-1 at 1 A g-1	16

Table S3. The values of R_s and R_{ct} for NPCF, Bi_2O_3@CC and Bi_2O_3@NPCF.

electrode	R_s	R_{ct}
NPCF	1.29	1.34
Bi_2O_3@CC	2.85	1.77
Bi_2O_3@NPCF	1.46	0.61

Table S4. Comparison of cyclic stability of Bi_2O_3@NPCF with other Bi-based/carbon nanocomposite supercapacitors

Electrodes	Current density	Cycle number	Capacity retention	References
Bi_2O_3@NPCF	40 mA cm^{-2}	10000	99.6 %	**This work**
P/Bi/C	40 mA cm-2	5000	74.5 %	[17]
rGO/Bi	100 mV s^{-1}	50000	83 %	[18]
AC-Bi_2O_3	---	1000	59 %	[5]
Bi_2O_3@C	5 A g^{-1}	4000	93 %	[19]
Bi_2O_3/CNFs	---	4000	92.21%	[20]
Bi_2O_3/C-1 NFs	---	4000	72.3 %	[20]
Bi_2O_3@C	500 mA g^{-1}	6000	50 %	[21]
Bi_2O_3/N-HPC	5 A g^{-1}	10000	85.2 %	[22]
Bi_2O_3@rGO	2 A g^{-1}	3000	99 %	[23]

Reference

(1) Kresse, G.; Furthmüller, J. Efficiency of Ab-Initio Total Energy Calculations for Metals and Semiconductors Using a Plane-Wave Basis Set. *Comput. Mater. Sci.* **1996**, *6* (1), 15–50. https://doi.org/10.1016/0927-0256(96)00008-0.

(2) Levämäki, H.; Kuisma, M.; Kokko, K. Space Partitioning of Exchange-Correlation Functionals with the Projector Augmented-Wave Method. *J. Chem. Phys.* **2019**, *150* (5), 054101. https://doi.org/10.1063/1.5078432.

(3) *Facile synthesis of BiSI and Bi13S18I2 as stable electrode materials for supercapacitor applications - Journal of Materials Chemistry C (RSC Publishing)*. https://pubs.rsc.org/en/content/articlelanding/2020/tc/d0tc02993a (accessed 2024-10-11).

(4) Xu, H.; Hu, X.; Yang, H.; Sun, Y.; Hu, C.; Huang, Y. Flexible Asymmetric Micro-Supercapacitors Based on Bi2O3 and MnO2 Nanoflowers: Larger Areal Mass Promises Higher Energy Density. *Adv. Energy Mater.* **2015**, *5* (6), 1401882. https://doi.org/10.1002/aenm.201401882.

(5) Wang, S. X.; Jin, C. C.; Qian, W. J. Bi2O3 with Activated Carbon Composite as a Supercapacitor Electrode. *J. Alloys Compd.* **2014**, *615*, 12–17. https://doi.org/10.1016/j.jallcom.2014.06.149.

(6) Prasath, A.; Athika, M.; Duraisamy, E.; Selva Sharma, A.; Sankar Devi, V.; Elumalai, P. Carbon Quantum Dot-Anchored Bismuth Oxide Composites as Potential Electrode for Lithium-Ion Battery and Supercapacitor Applications. *ACS Omega* **2019**, *4* (3), 4943–4954. https://doi.org/10.1021/acsomega.8b03490.

(7) Shinde, N. M.; Xia, Q. X.; Yun, J. M.; Mane, R. S.; Kim, K. H. Polycrystalline and Mesoporous 3-D Bi2O3 Nanostructured Negatrodes for High-Energy and Power-Asymmetric Supercapacitors: Superfast Room-Temperature Direct Wet Chemical Growth. *ACS Appl. Mater. Interfaces* **2018**. https://doi.org/10.1021/acsami.8b00260.

(8) Khan, Z.; Bhattu, S.; Haram, S.; Khushalani, D. SWCNT/BiVO4 Composites as Anode Materials for Supercapacitor Application. *RSC Adv.* **2014**, *4* (33), 17378–17381. https://doi.org/10.1039/C4RA01273A.

(9) Zheng, F.-L.; Li, G.-R.; Ou, Y.-N.; Wang, Z.-L.; Su, C.-Y.; Tong, Y.-X. Synthesis of Hierarchical Rippled Bi2O3 Nanobelts for Supercapacitor Applications. *Chem. Commun.* **2010**, *46* (27), 5021–5023. https://doi.org/10.1039/C002126A.

(10) Wang, Y.; Zhang, T.; Zheng, X.; Tian, X.; Yuan, S. Enhancing Energy Storage via Confining Sulfite Anions onto Iron Oxide/Poly(3,4-Ethylenedioxythiophene) Heterointerface. *ACS Appl. Mater. Interfaces* **2023**, *15* (51), 59413–59421. https://doi.org/10.1021/acsami.3c13148.

(11) Saravanakumar, B.; Purushothaman, K. K.; Muralidharan, G. V2O5 / Nitrogen Enriched Mesoporous Carbon Spheres Nanocomposite as Supercapacitor Electrode. *Microporous Mesoporous Mater.* **2018**, *258*, 83–94. https://doi.org/10.1016/j.micromeso.2017.09.010.

(12) Tian, S.; Zhang, B.; Han, D.; Gong, Z.; Li, X. Fe2O3/Porous Carbon Composite Derived from Oily Sludge Waste as an Advanced Anode Material for Supercapacitor Application. *Nanomaterials* **2022**, *12* (21), 3819. https://doi.org/10.3390/nano12213819.

(13) Gueon, D.; Moon, J. H. *MnO2 Nanoflake-Shelled Carbon Nanotube Particles for High-Performance Supercapacitors*. ACS Publications.

https://doi.org/10.1021/acssuschemeng.6b02803.

(14) Ray, S. K.; Kokayi, M.; Desai, R.; Dahal, R.; Ashie, M. D.; Mantripragada, S.; Bastakoti, B. P. Ni/NiO Nanoparticles Loaded Carbon Sphere for High-Performance Supercapacitor. *Mater. Chem. Phys.* **2024**, *320*, 129403. https://doi.org/10.1016/j.matchemphys.2024.129403.

(15) Li, S.; Zhang, L.; Zhang, L.; Guo, Y.; Chen, X.; Holze, R.; Tang, T. Preparation of Fe3O4@polypyrrole Composite Materials for Asymmetric Supercapacitor Applications. *New J. Chem.* **2021**, *45* (35), 16011–16018. https://doi.org/10.1039/D1NJ02957F.

(16) Kim, H. S.; Kang, M. S.; Yoo, W. C. Co3O4 Nanocrystals on Crab Shell-derived Carbon Nanofibers (Co3O4@CSCNs) for High-performance Supercapacitors. https://doi.org/10.1002/bkcs.11389.

(17) Zeng, Y.; Lin, Z.; Wang, Z.; Wu, M.; Tong, Y.; Lu, X. In Situ Activation of 3D Porous Bi/Carbon Architectures: Toward High-Energy and Stable Nickel–Bismuth Batteries. *Adv. Mater.* **2018**, *30* (18), 1707290. https://doi.org/10.1002/adma.201707290.

(18) Wang, M.; Xie, S.; Tang, C.; Fang, X.; Liao, M.; Wang, L.; Zhao, Y.; Wen, Y.; Ye, L.; Wang, B.; Peng, H. In Situ Intercalation of Bismuth into 3D Reduced Graphene Oxide Scaffolds for High Capacity and Long Cycle-Life Energy Storage. *Small* **2019**, *15* (52), 1905903. https://doi.org/10.1002/smll.201905903.

(19) Yu, X.; Sun, J.; Zhao, W.; Zhao, S.; Chen, H.; Tao, K.; Hu, Y.; Han, L. MOF-Derived Bi2O3@C Microrods as Negative Electrodes for Advanced Asymmetric Supercapacitors. *RSC Adv.* **2020**, *10* (24), 14107–14112. https://doi.org/10.1039/D0RA01470B.

(20) Wang, Y.; Zhou, J.; Chen, K.; Zhao, W.; Tao, K.; Han, L. Metal–Organic Framework-Derived Bi2O3/C and NiCo2S4 Hollow Nanofibers for Asymmetric Supercapacitors. *ACS Appl. Nano Mater.* **2021**. https://doi.org/10.1021/acsanm.1c02475.

(21) Oli, N.; Ortiz Lago, W.; Tripathi, B.; Bhattarai, M.; Weiner, B. R.; Morell, G.; Katiyar, R. S. Enhanced Electrochemical Performance of Bi2O3 via Facile Synthesis as Anode Material for Ultra-Long Cycle Lifespan Lithium-Ion Batteries. *Electrochem. Commun.* **2024**, *159*, 107656. https://doi.org/10.1016/j.elecom.2023.107656.

(22) Zhu, W.; Shen, D. Synthesis of Bi2O3/Hierarchical Porous Carbon Composites for Supercapacitor Application. *J. Energy Storage* **2024**, *79*, 110118. https://doi.org/10.1016/j.est.2023.110118.

(23) *Performance evaluation of Bi2O3@GO and Bi2O3@rGO composites electrode for supercapacitor application | Journal of Materials Science: Materials in Electronics*. https://link.springer.com/article/10.1007/s10854-023-10835-7 (accessed 2024-10-11).